UNIVERSITY OF CALIFORNIA,
IRVINE

Improved Fabrication of Plasmonic Structures

THESIS

submitted in partial satisfaction of the requirements
for the degree of

MASTER OF SCIENCE

in CHEMISTRY

by

Nicholas Sharac

Thesis Committee:
Associate Professor Regina Ragan, Chair
Chancellor's Professor Reginald Penner
Professor John Hemminger

2014

TABLE OF CONTENTS

LIST OF FIGURES

LIST OF TABLES

ACKNOWLEDGMENTS

I would like to thank my chair and Principal Investigator, Professor Regina Ragan, for her continual support and advice; my committee members, Professor Reginald Penner and Professor John Hemminger for their patience; Professor Michelle Khine and Dr. Himanshu Sharma for their collaborative efforts regarding the thermoplastic based work mentioned in this manuscript; the National Science Foundation CHE-0748912 and CMMI-1101074 for funding; and Dr. Joshua Caldwell at the Naval Research Laboratory for allowing me to partake in the Silicon Carbide work for my summer internship and for funding.

I thank the Royal Society of Chemistry, The American Chemical Society, and SPIE for Permission to include copyrighted figures as part of my thesis dissertation.

ABSTRACT OF THE THESIS

Improved Fabrication of Plasmonic Structures

By

Nicholas Sharac

Master of Science in Chemical and Material Physics for Chemistry

University of California, Irvine, 2014

Professor Regina Ragan, Chair

Periodic metal nanostructure arrays possess electromagnetic properties useful for metamaterials, light trapping, and molecular sensing, such as surface enhanced Raman spectroscopy (SERS). The localized plasmon resonance frequency of these arrays depends on the material, periodicity, size, and spacing of nanoparticles. While bottom down fabrication techniques are often inexpensive and more realistic on a manufacturing scale than top down fabrication alternatives, tuning nanostructure parameters to modify optical properties is currently limited. In my work, I have demonstrated the potential for scaling down and tuning nanostructures fabricated by bottom up techniques, by using a thermally responsive polyolefin (PO) film in conjunction with nanosphere lithography (NSL). By heating the patterned substrate in a convection oven, I have successfully fabricated both nanopillar arrays with tunable dimensions, which can be used in antireflective applications, and tunable gold nanotriangle arrays, which have previously been shown to generate SERS enhancements due to the hot spots between two tips. Reductions in area as great as 95% have been achieved. Reflectance spectroscopy shows the tunabilty of the triangle array to tune the plasmon resonance. These findings are confirmed by subsequent SERS experiments. I also present here work on localized surface phonon polariton modes (SPhP),

which are potential low loss alternative to plasmonics. 6H-silicon carbide nanopillar arrays are fabricated to generate localized SPhP modes, which are measured using FTIR reflectance spectroscopy and Raman spectroscopy. The measured SPhP modes are found to have exceptionally narrow line widths, giving high Q factors and low losses, and in many cases are Raman active.

INTRODUCTION

Surface plasmons are collective electric charge oscillations at the interface of a metal and dielectric [1-3]. Incident light in the visible and near- IR range can couple with surface plasmons, resulting in surface plasmon polaritons, which propagate along the metal dielectric surface in a wave until absorbed by a metal or radiated into space. Surface plasmon resonance occurs when plasmons are hit by light of the same frequency as in the plasma, called resonance frequency. In sub-wavelength sized metal structures, this phenomenon is localized, and is known as localized surface plasmon resonance. The localized plasmon resonance can be tuned by changing the size, shape, periodicity, and metal of the nanostructure.

Tuning the localized surface plasmon resonance in noble metal structures is pivotal in optimizing a wide range of applications, such as nanophotonic devices[4-9], biological sensors[10, 11], and photovoltaics[12]. The highest enhancement factors for surface enhanced Raman spectroscopy (SERS)[13] and metal enhanced fluorescence (MEF) [14] , currently greater than 1x10^9 [15] and 1,100 fold[16],respectively, are attained when the plasmon frequency is between the frequency of the incident light and that of the light scattered from the analyte molecule[17,18], or in the case of MEF, the light emitted from the fluorophore. Single molecular detection, perhaps currently the single largest goal in bio sensing devices, can be attained by SERS for plasmonic enhancement factors in hot spots exceeding 10^{10}[19]. For solar cell devices, enhancing light absorption in the solar frequency range allows for the highest increases in efficiency [20]. Additionally, dielectric structures with anti-reflective (AR) properties have shown promise in increasing absorption for solar cells and transmittance for light-emitting diodes (LED) [21]. Plasmonics also have applications in light screens, solar

devices, thermal cancer treatment, catalysis, and are the precursors for metamaterials, which has a host of new applications itself.

Current progress in plasmonics is limited by: 1) The high expense and low throughput of current manufacturing techniques, discussed below, 2) the smallest attainable feature sizes from those techniques, 3) the lack of control offered by cheaper, more robust techniques, 4) Inherently high losses in metallic nanostructures.

The current state of the art processes for manufacturing plasmonic devices all utilize electron beam (e-beam) lithography [22]. E-beam lithography works similar to a scanning electron microscope (SEM), where a beam of electrons is rastered across a surface coated with photoresist. The exposed photoresist can then be treated similar as in other photolithographic processes. Advantages in e-beam lithography include direct control of the pattern, using writing programs, below the diffraction limit. Feature sizes can reproducibly be made down to 10 nm, at best, though state of the art cases using an aberration corrected STEM have reported sizes down to 2 nm [23]. However, consistent pitch and feature spacing are more difficult to attain due to secondary electron scattering, thermal noise, and vibrations. The biggest drawbacks of e-beam are its high cost and low throughput. Direct writing machines cost several million dollars-the conversion of an SEM to an e-beam lithography system still requires around $100,000 in addition to the cost of the SEM. Throughput is currently low, due to the linear nature of the e-beam process and is currently on the scale of hours per wafer.

E-beam is an example of top down lithography, where a pattern is sculpted from a larger building block. Bottom up lithography, in contrast, creates a pattern from smaller building blocks. Molecular self-assembly is perhaps the most common bottom up method, and is found in nature, for instance in helical bonding in the DNA[24]. Molecular units organize into ordered

structures through molecular interactions. Self- assembly occurs for larger particles as well, such as in nanosphere lithography (NSL), which utilizes the close packing of polystyrene and silica microspheres [25]. Bottom up methods offer faster, cheaper solutions, with higher coverage, but often at the cost of tunability. For instance, in work by Park, nanopillar arrays, in close resemblance to the cones in a moth's eye, were fabricated on both sides of glass using NSL, resulting in a 99% transparency in the visible region [26]. By tuning the height and pillar shape, they were able to tune the frequency region in which the AR properties occurred. However, the spacing between pillars, which plays a direct role in the refractive index gradient, remained fixed, due to the inherent inability of NSL to alter periodicity independently of structure height and size. Ideally, a scaling method would be realized which can improve the deficiencies in both nanofabrication approaches, to reduce the feature and pitch sizes attained by state of the art techniques and those attained by larger, higher coverage methods, in addition to offering quick, facile tunability. The fourth limitation mentioned above is directly related to high loss in noble metal structures [27]. Even the best plasmonic systems today are still limited in terms of practicality due to the high losses inherent in noble metals, which have high absorbances. This poses the biggest concern for waveguiding applications, as it transmit signals across a device but even for other applications, such as sensing, it has been speculated that lower loss alternatives with stronger, sharper resonances would offer even better sensitivity [28].

In my research, I have addressed the first three mentioned problems (cost, minimum feature size attainable, and versatility) by developing an inexpensive, ease of use technique for tunable structures which can be potentially applied to a wide range of bottom up and top down techniques. Additionally, I have addressed the fourth problem (loss) by exploring alternative, low loss photonic systems in the form of silicon carbide (SiC) nanopillar arrays. In the former

case, I have combined nanosphere lithography (NSL), a robust, bottom up technique, with a polyolefin thermoplastic substrate, a technology only recently being realized for engineering applications, and in terms of lithography, still far in its infancy [29]. With these two combined techniques, I have produced nanopillars and gold nanotriangles, which are attainable via traditional nanosphere lithography, and have reduced both these patterns, through heating, by up to 95% in surface area. The tunability of our substrates is showcased in several ways. First, we show the independent parameterization of our nanopillar structures, by independently changing the pillar diameter and periodicity [30], which in traditional NSL is not possible. Second, we show the possibility of asymmetric stretching, which allows for a wider array of different patterns to be realized. Finally, with our triangles, we show that reducing the periodicity and size of our structures can tune the plasmon resonance, with a window of at least 100 nm. All these modifications offered by our new substrate can be done within an hour. Showing the ability of the thermo plastic to tune and reduce two very different nano patterns, with gap sizes as low as 5 nm remaining intact, is a promising start for the utilization of this technique with other fabrication processes, including E-beam. Additionally, I have participated in the investigation of a polar dielectric based alternative to plasmonics, realized through electron beam lithography, to create silicon carbide nanopillar arrays, with potential use in SERS and surface enhanced infrared absorption spectroscopy (SEIRA) [31].The long lifetime of surface phonon polar modes allow for low loss materials. In chapter 2, I detail the wok performed with the thermoplastic film, discussing first the fabrication and tunability of nanopillar structures, followed by the fabrication and tunability of nanotriangle arrays. Finally, I discuss the implications of the work, and where these findings can next be applied. In chapter 3, I detail my work on SiC nanopillar structures, the nature of localized SPhP modes, and the potential progress of this field in the near future.

2. Versatile nano self-assembly using a thermoplastic film

Thermoplastic substrates are initially prestressed plastic films, which reduce to their original dimensions when heated. These films have been exploited in the last few years to produce wrinkled metallic nanostructures for MEF, in work by Sharma et al. [32]. This was accomplished by coating the thermoplastic with a metal layer, which buckles as the surface area of the substrate is reduced. In similar work by Zhang et al[33], a polystyrene film (PS) was used to generate wrinkled nanoporous Au/Ag films, generating hot spots with SERS enhancements factors over 10^9, high enough for single molecule detection. However, the frequency and location of hot spots generated from the metal wrinkles are not controllable. Furthermore, the wrinkled nature of the metal wrinkle film limits the number of applications that can be used. Ideally, the film can be used to generate small spacings in a controlled manner, by combining the heat shrink film's properties with traditional lithography. This opens up the film's potential for a wide ranger

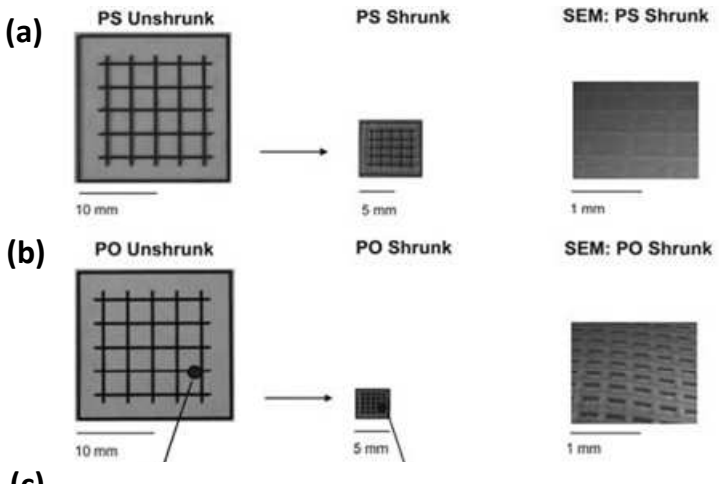

(c)

	% Change in Area	% Change in X	% Change in Y	% Change in Horizontal Line Width	% Change in Vertical Line Width	Shrunk Line Height (μm)
Average	94.87	77.43	77.29	45.00	40.82	47.54
Standard Deviation	0.51	1.10	1.88	8.82	9.66	11.70

Fig 1. A PS film (a) and PO film (b) with ink jet printed lines are placed in a convection oven to reduce their x and y dimensions, while preserving the shape of the original pattern. e) shows the % change in the x and y dimensions of the printed lines for the PO film, which is 77% for both directions. [29]

range of applications, including controlled biosensing, AR reflective properties, and even potentially metamaterial substrates. Nguyen et al. has shown proof of concept of this possibility, using an ink jet printer, that the polyolefin film can be used to reduce patterns by 95% in surface area and 77% in length [28], while maintaining the X and Y dimensions. However, this experiment was limited to the macro scale. I show here that the polyolefin's pattern reduction capability can be utilized even at the nanoscale. Ideally this can be applied as an added feature to optimize bottom up techniques, and also to attain difficult, complicated structures that require spacings smaller than that attainable by EBL.

I have employed nanosphere lithography for its ease of use and low cost, in order to demonstrate the potential use of thermoplastics in nanofabrication processes. In nanosphere lithography (NSL), spheres of diameters of 500 nm to several μm are deposited onto a surface in a colloidal suspension. Evaporation of the solvent causes the spheres to hexagonally close pack to preserve energy. Beads can also pack in layers, in either ABA stacking, or ABCA stacking. Close packing is controlled by concentration of the solution, sphere size, surface energy of the substrate, and rate of evaporation of the solution. Spheres are typically silica or polystyrene. The forces that pack the spheres are convective and capillary, depending on the method of deposition (dip coating, spin coating, doctor blading, etc.).The beads are then used as a mask, as in traditional photolithography, where the exposed regions of the substrate underneath it are either coated with metal, or etched. The beads can then be removed via sonication in water or ethanol. NSL has been used to generate various patterns, as shown in Fig. 2, among them, using RIE and plasma etching, nanopillars, and, using metal vapor deposition, nano triangles, also known as the bow tie structure. The main limiting factors of NSL lie in the mask itself. 1) Periodicity and nanostructure size cannot be independently tuned. 2) Bead diameters below ~200 nm are difficult

to pack in the HCP structure, due to increased Brownian motion and decreased monodispersity. This severely limits the smallest feature sizes attainable.

By applying nanosphere lithography to a plastic PO substrate, we have developed a low cost, robust, high throughput and versatile technique to fabricate arrays of two types of nanostructures, both nanopillar arrays and the bow tie structure, and are able to reduce the former pattern by ~35% and the latter by ~77%. Further, we improve the NSL technique by showing independent tuning of periodicity and feature size, with the added benefit of additional size reduction, post fabrication, of the initial NSL structures. In terms of application, I show the potential of tunable bow tie arrays, by modifying the maximum SERS EF as a function of heat.

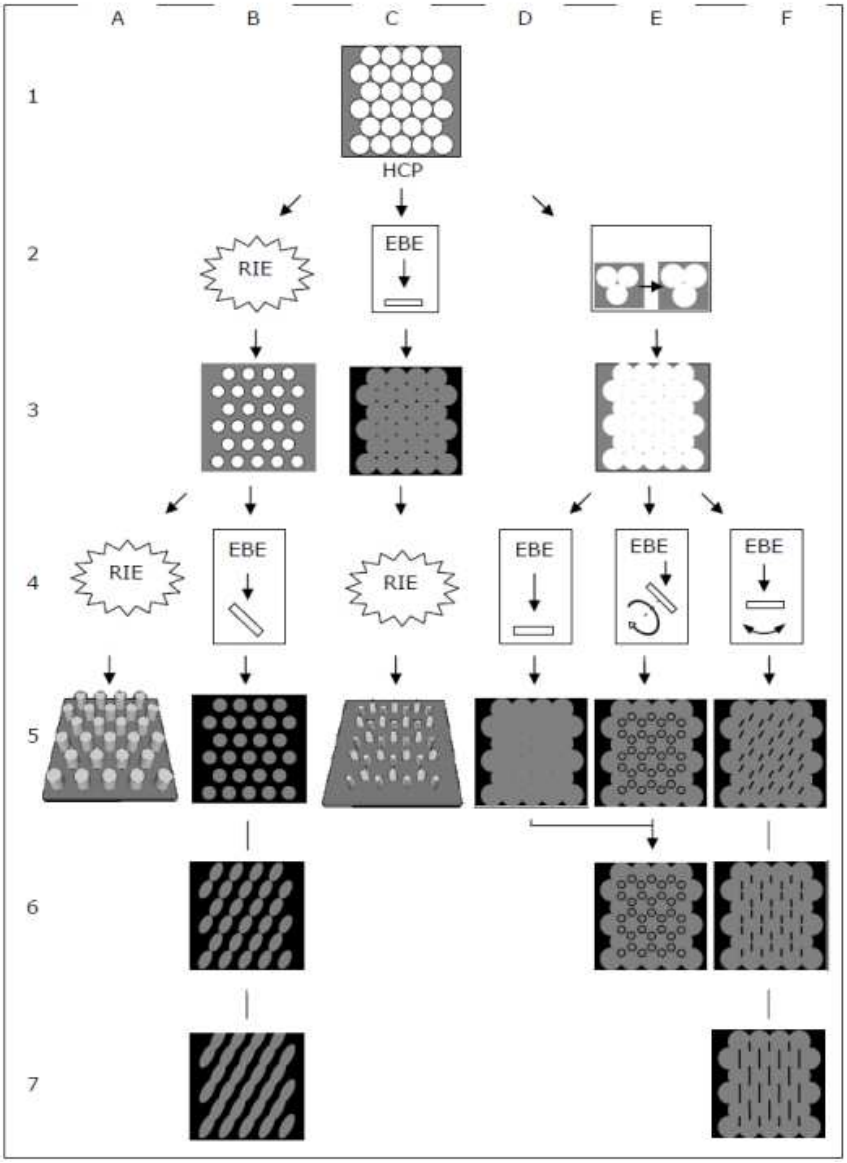

Fig 2. Examples of possible nanostructures arrays that can be fabricated using nanosphere lithography [25].

Reprinted with permission from A. Kosiorek ,† W. Kandulski ,† P. Chudzinski ,‡ K. Kempa ,§ and M. Giersig *† "Shadow Nanosphere Lithography," ,*Nano Lett.* vol. 4, no. 7, pp. 1359-1363,2004. American Chemical Society.

2.1 Tunable nanopillar arrays

Nanopillar arrays have shown potential use in solar, anti-reflective coatings, and SERS enhancements. For instance, Caldwell et all, has used e-beam lithography to generate gold nanopillar arrays, with diameters ranging from 320 nm to 120 nm and distances from 270 nm to 60 nm, for a tunable plasmon resonance, with uniform SERS enhancement factors as high as ~1.2x10^8 [34]. Park et al. has used NSL to generate nanopllars in close resemblance to the cones in a moth's eye, on both sides of glass using NSL, resulting in a 99% transparency in the visible region. By tuning the height and pillar shape, they were able to tune the frequency region in which the AR properties occurred. The AR properties arise from periodic structures smaller than the wavelength of light, which results in a smooth gradient in the refractive index and an effective absence of an air lens interface [26].However, the spacing between pillars, which plays a direct role in the refractive index gradient, remained fixed, due to the inherent inability of NSL to alter periodicity independently of structure height and size

I am able to produce nanopillar arrays similar to the work done by Park, but with the significant difference of facile tunability. The nanopillars discussed next do not require EBL to alter periodicity, and can be tuned in under an hour. This is useful for experiments that are pitch dependent, such as the moth eye structure. By using nanosphere lithography in conjunction with the PO film, these bead-pillars are reducible in periodicity. Additionally, plasma etching supplies another independent parameter to vary the size of PS and the height of nano bead-pillars. The process is shown in Fig. 3. NSL provides a hexagonal closed packed mask of latex beads of 500 nm diameter. Introducing the beads and PO substrate to oxygen plasma allows for tuning of the beads diameter and spacing, in addition to creation of pillar structures from the etched PO. The substrate, consisting of a polyolefin blend, is pre-stressed, and therefore reduces in surface area when exposed to temperatures above 100 °C. This is used to modify the geometry of our pillar

array. Overall the spacing, feature size and height of these nano pillars can be tuned independently by thermal processing and plasma etching. Finally, gold can be added to our pillars via physical vapor deposition (PVD).

2.1.1 Experimental

Polyolefin (PO) films (955-D, Sealed Air Corporation) ,with thickness of approximately 1 millimeter that are laminated on a 3 millimeter polyester backing ,are cleaned in isopropyl alcohol and then dried with pressurized air. The clean PO film is then oxygen plasma treated for 30 s at a power of 60 W to increase the hydrophilicity of PO surfaces. A solution of 500 nm polystyrene (PS) beads (Bangs lab) was diluted to a 3:1 ratio with triton X-100 and methanol (1:400 by volume). Approximately 12 µL of this solution was then spin coated onto the PO film for 5 minutes at 1000 RPM and allowed to dry for two hours. After spin coating, the substrate is plasma etched at a power of 60 W in an Oxygen plasma asher for different times, from 540s to 810 s. Immediately following the plasma etch step, samples are sonicated in ethanol for one minute and subsequently sonicated in deionized (DI) water for thirty seconds to remove residual etchant material. The samples are then mounted on a glass slide with double sided tape and

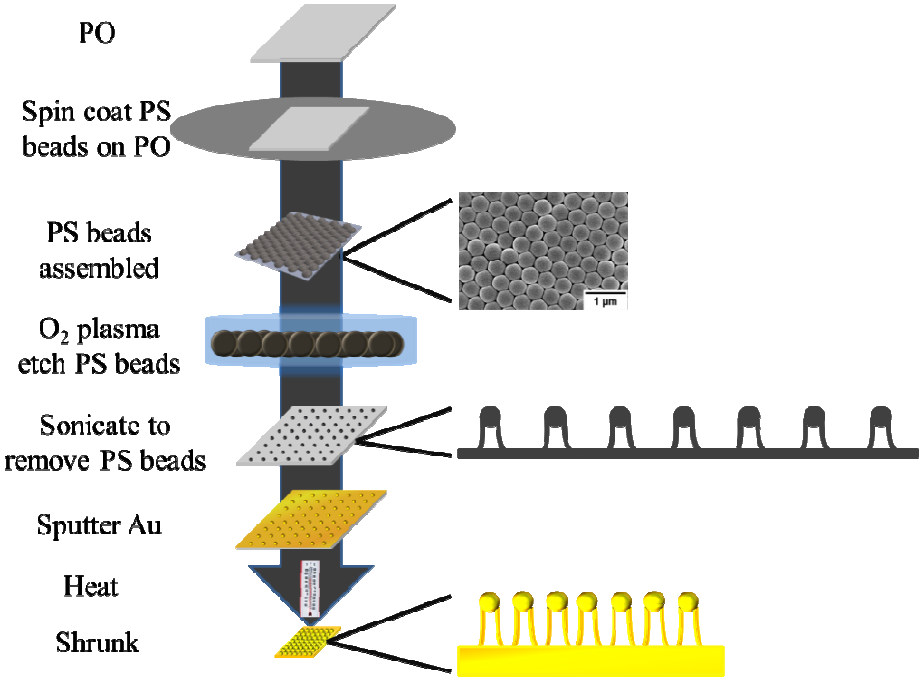

Figure 3. Schematic process flow for fabrication of nano bead pillars.

Reprinted with permission from N. Sharac, H. Sharma, M. Khine, R. Ragan. "Tunable nano bead arrays on film for controlling propogation of light," *SPIE proceedings*, vol. 8809, 2013.

heated in a convection oven from room temperature to different degrees of temperature ranging from 90 °C to 120 °C. The differences in the length from the original PO size were measured with a digital caliper during the heating process. The percentages shrunk in length were calculated by taking the ratio of the final width of substrate relative to the initial width. Finally, samples were coated with a 5 nm titanium adhesion layer followed by 50 nm Au, using chemical vapor deposition. Temperatures did not exceed 115° C during this process to avoid further shrinking. An atomic force microscope (AFM) (Asylum Research MFP-3D AFM) with silicon cantilevers (Olympus) was used to characterize the resulting topography of our substrate, and a scanning electron microscope (SEM) (FEI- Magellan 400 XHR), at ~ 2 kv, was used to image the periodicity of features over a large area.

2.1.2 Results

The oxygen plasma etch time was varied to determine the etch rate of PS beads and the underlying PO. SEM images, after etching, are shown in Figure 4 a-d etched for time periods of (a) 540 s, (b) 630 s, (c) 720 s, (d) 810 s, respectively, since plasma etching the PS beads was found to be most effective in this time range. Etching times less than 540 s

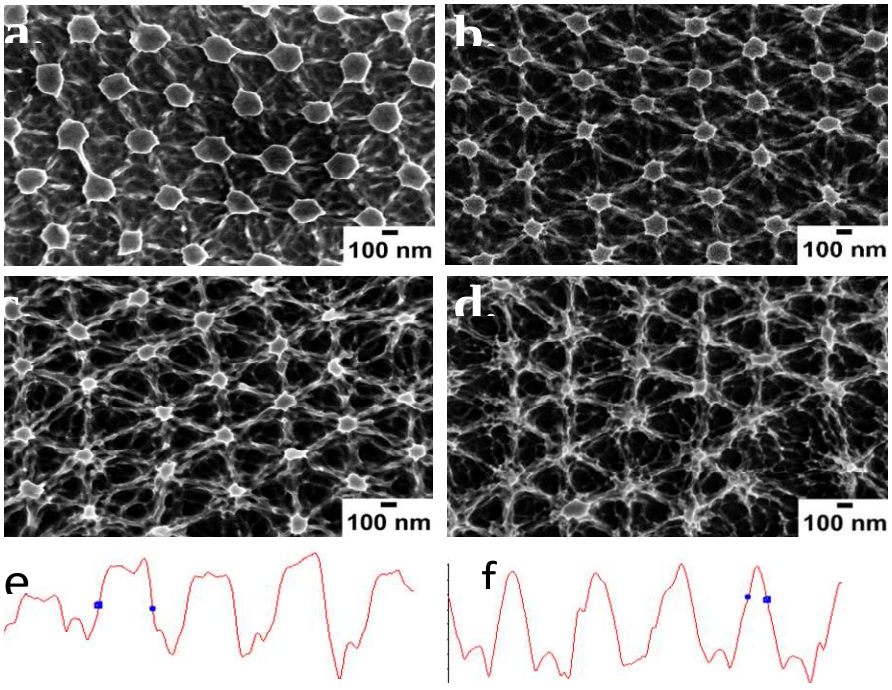

Figure 4. SEM images of gold coated 500 nm PS bead arrays that were reduced in size using various plasma etch times: a) 540 s, b) 630 s, c) 730 s, d) 810 s. Scale bar is 100 nm. 2 µm AFM height profiles for samples etched for e) 540 s, and f. 810 s provide the shape of the resulting nanopillar beads.
Reprinted with permission from N. Sharac, H. Sharma, M. Khine, R. Ragan. "Tunable nano bead arrays on film for controlling propogation of light," *SPIE proceedings*, vol. 8809, 2013.

resulted in minimal etching of PS beads, and beyond 810 s, the pillars were found to be damaged in SEM images, data not shown. Etching for time periods of 540-810 s led to a deformation of PS beads, as observed in Fig. 4. Etch times longer than 810 s led to significant etching of PS beads to the point of obliteration. Fig. 4d, shows the PS beads to be significantly smaller and distorted when compared to Fig. 4a, 2b, and 4c. As expected, as the diameter of nano pillars is reduced due to increasing the etch time, the inter-spacing between the pillars is increased as observed in Figure 4 a-d. As the measured pillar width decreased from approximately 240 nm to 100 nm, when the etch time increased from 540 to 810 s, the edge to edge spacing increased from approximately 250 nm to 400 nm. AFM topography line profiles are shown in Fig. 4 e and 2f, corresponding to etch times of 540s and 810 s, respectively. The height profiles illustrate that with longer etch times, the top point of the pillars becomes sharper relative to the smooth tops observed on pillars after an etch time of 540 s, observed in both in Fig. 4 e and 4f.

AFM topography images of the etched beads are shown in the first row of Figure 5, with a common height scale legend on the right show that heights range from approximately 60 nm for pillars etched for

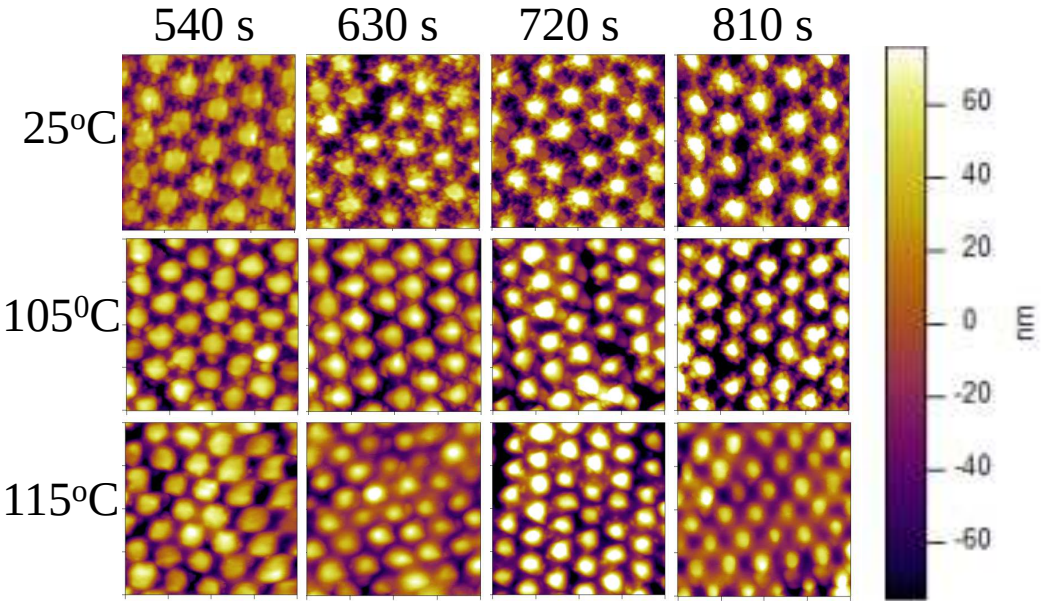

Figure5. AFM topography images of gold coated PS bead arrays on PO, etched for different time intervals and then shrunk in size from 0% to 20% to 33% by heating them from 25°C to 105°C to 115°C, respectively.

540 s and up to 160 nm for a plasma etch time of 810 s and that the height increase is monotonic with etch time. Due to the diminished beads after 810s of plasma etching, while the etched PO film was still intact, further deepening of the pillar features on the surface was not possible due to the obliteration of the PS NSL mask. If a higher aspect ratio is needed, RIE can be used, due to the difference in dry etch rates between PO and PS [35, 36]. This is especially important for plasmonic applications where high aspect ratio structures are correlated with strong local electric fields [37] or for anti-reflection applications such as "moth eye" structures, where height has been shown to play a major role in AR, due to suppression of light reflection. Traditionally, NSL has been performed on Si substrates to generate pillars with heights up to 400 nm by using selective etching methods, such as RIE, with fluorination or chemical etchants. On such a hard surface, the beads do not adhere to the surface and are removed after sonication in a solvent. Using a soft PO film, the PS beads remain bound to the PO film surface. Also, the beads appeared to have a strong adhesion to the PO surface. Sonicating the PS coated PO films in organic solvents such as hexanes and dichloromethane did not lead to release of PS beads. If combined with selective etching, tall, high aspect pillars can be attained with easily shapeable caps.

We also investigated how a combination of etching and thermal processing leads to independent control of feature size and periodicity not obtained in conventional NSL. Fig. 5 shows AFM topography images for PS bead arrays on PO, etched for different durations and heated from room temperature to 105° C and 115^{o}C. Visually, it can be observed in the AFM images that as the substrate is heated, the spacing between nanopillars decreases, with this decrease correlated with the percentage of decrease in dimensions of the PO substrate. Furthermore, thermal processing also increases the heights of the nano bead pillars by

approximately 30 nm when heated to 115°C. Based on the conservation of mass law, since film contracts in the X and Y direction, the film must increase in the Z direction. Approximately 30 nm increase in the height was observed when shrinking to approximately 35% in length for all the etch times. Although the PO film has the ability to contract by up to77% in length by heating to 155^{o}C, the substrates were only shrunk to approximately 35% in length at T = 115 °C. The limit in thermal processing and achievable reduction in feature size, as has been previously demonstrated, is due to stiffening of the PO surface during etching. With the addition of the thin oxide layer attained during plasma etching and metal deposition, shrinking the PO film past 35% in length forced wrinkles to form. This was clearly evident in the SEM and AFM images where the bead pillar arrays became masked by the wrinkles or the features were not all in one plane. A summary of the differences in the widths, heights, and distances measured for the substrates is presented in Table 1. For a more quantitative analysis, the same values are also plotted as a function of etch time shown in Fig. 4. It is important to note that the spacings reported were measured from center to center, and therefore no decrease in distance as a function of etch time is shown here.

Etch time (s)	**Shrink Temp (^{o}C)**	**Width (nm)**	**Spacing in x (nm)**	**Spacing in y (nm)**	**Height (nm)**
540	25	237 ± 6	452 ± 11	448 ± 10	65 ± 4
540	105	224 ± 5	366 ± 10	384 10	79 ± 3
540	115	215 ± 14	314 ± 9	375 ± 15	85 ± 4
630	25	123 ± 7	451 ± 14	429 ± 19	100 ± 6
630	105	118 ± 7	381. ± 4	376 ± 5	120 ± 7
630	115	119 ± 9	314 ± 4	351 ± 6	125 ± 4
720	25	128 ± 8	438 ± 12	445 ± 10	97 ± 5
720	105	128 ± 4	381 ± 9	380 ± 10	105 ± 6
720	115	126 ± 2	343 ± 10	294 ± 9	113 ± 4
810	25	95 ± 7	439 ± 11	452 ± 9	124 ± 5
810	105	97 ± 5	386 ± 7	356 ± 6	132 ± 4
810	115	92 ± 7	320 ± 11	330 ± 8	143 ± 6

Table 1. Gap spacing, height, and width dimensions of PS bead arrays for different etch times and shrink temperatures.

Reprinted with permission from N. Sharac, H. Sharma, M. Khine, R. Ragan. "Tunable nano bead arrays on film for controlling propogation of light," *SPIE proceedings*, vol. 8809, 2013.

As presented in Table 1 and illustrated in Fig. 6, the nanopillars do not vary much in width after heating. In theory, shrinking the substrates should result in smaller diameter of the pillars. This may be related to the PO being segmented into small areas when etched into pillars, preventing the normal shrinking expected. As shown in Fig.4, only the largest measured pillars appear to shrink to a small extent with increase in temperature. This may be due to the segmented PO still being large enough to decrease in surface area to some small extent. As expected, the center to center spacings decreased as a function of heat, as shown in table 1 and Fig. 6, from approximately 450 to 300 nm, which is approximately a 35% reduction in distance. This reduction in spacing corresponds well to the measured reduction in the length of our plastic substrates. Fig.4 also shows some variation exists in shrinking in the x and y directions of the substrate, which can be attributed to asymmetric stretching of the substrate. Achieving control over this asymmetry is possible by constraining the sample in one direction while heating. The constrained side can be alternated according to desired shrink percentage and desired level of asymmetry. Control of the asymmetry will allow more tunability in nanostructure arrays in addition to keeping the periodicity consistent. An interesting observation to note is that the samples etched for 810 s showed a continual decrease in the variation of periodicity for the x and y directions as heat was increased.

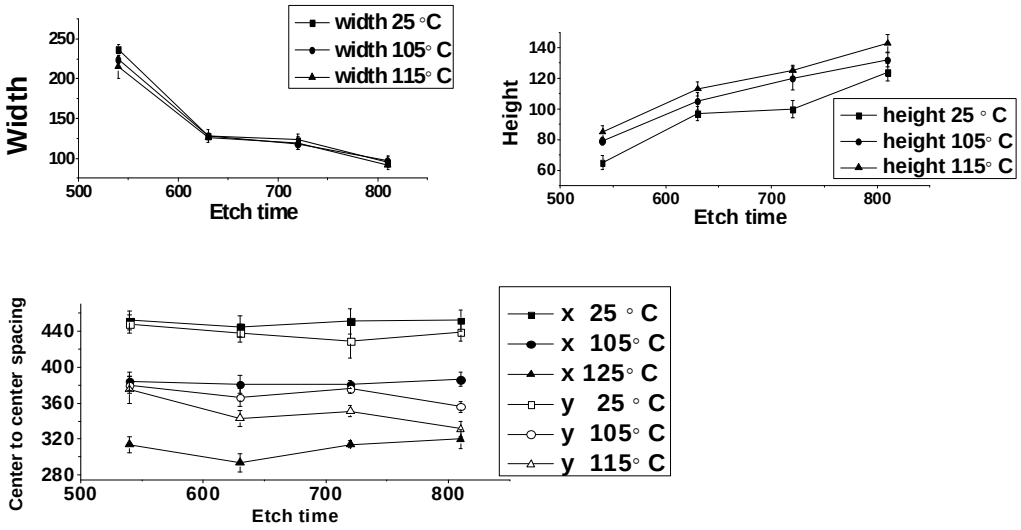

Figure 6. Spacing, width, and heights for PS bead arrays shown as a function of etch time and shrink temperatures.
Reprinted with permission from N. Sharac, H. Sharma, M. Khine, R. Ragan. "Tunable nano bead arrays on film for controlling propogation of light," *SPIE proceedings*, vol. 8809, 2013.

2.1.3 Summary

In summary, I have developed a versatile method for quick, robust, and inexpensive fabrication of nanopillar structures. The thermoplastic PO substrate allows for facile tunability of inter particle spacing and height of the structures. Thermoplastics, combined with etching, provides a quick solution to achieve wide range of pillar widths and interpillar spacings. Most significantly, I have achieved independent parameterization of both pillar width and interpillar spacing. Currently, wrinkling prevents the substrates from shrinking past 35%, but this may be circumvented by first removing the oxide layer or by using a different heat film. Other etch methods, such as RIE, will be used in the future to create a deeper etch, resulting in taller pillars more suitable to AR properties. High aspect ratios in conjunction with increased height from shrinking, change in shape, and controlled variability in spacing should allow for the extensive study of AR properties in moth wing structures

2.2 Nanotriangles

Nanotriangles, also known as bowtie structure, are a common bottom up assembly pattern achieved by nanosphere lithography, which are fabricated by depositing metal through the interstices of the polystyrene sphere mask on the substrate, followed by mask lift off [25]. Previous work has shown hot spots to exist between the junction of two such Ag nanotriangles, with reported SERS enhancement factors over 10^7 [38] for Ag triangles, with 200 nm base length and 55 nm thickness. In this case, he used a tunable laser to match the incident and Raman scattered photons with the LSPR mode. The hot spots were reportedly from the triangle tips, due to the so called "lightning rod effect." Since the nanotriangles are a direct result of the metal deposited within the nanosphere spacings, the size of the triangles are directly dependent on the size of the latex spheres, where NSL is limited to HCP packing of 200 nm spheres at the smallest. This implies a limit on the size of the triangle, periodicity, and density, and as a result, the strength of the confined field. A thermoplastic substrate can bypass this limit. Here, I have reproduced similar nanotriangle arrays, using gold, with the added benefit of the polyolefin thermoplastic substrate. Unlike the aforementioned nanopillars, the nanotriangle design requires minimal oxygen plasma etching, minimizing the oxide layer and allowing for further size reduction of our polymer without wrinkles. The PO substrate enables the reduction of the tip to tip spacing by 77%, which enables the future possibility of plasmon coupling, as tip to tip spacings are shown in some cases as small as 1 nm. Futhermore, the reduction of the bowtie array size has been shown to blue shift the plasmon resonance, which is useful for fluorophore selectivity in metal enhanced fluorescence. The PO substrate allows for tunability of the periodicity, in addition to the size of the triangles. I use reflectance spectrometry and surface

enhanced Raman spectroscopy to show controllability of the plasmon resonance with size reduction in our nanotriangle arrays, where heating our arrays gives up to a maximum of 77% reduction in periodicity. Additionally, decreasing the intertip distance of the nanotriangles gives the potential bonus of increased enhancements within those hot spot regions.

2.2.1 Experimental

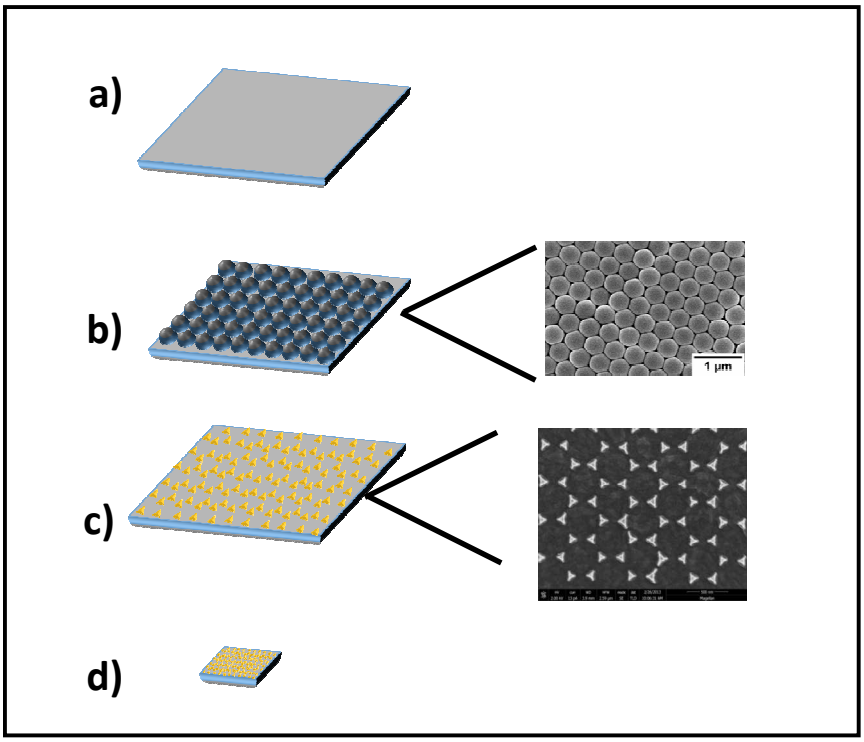

Fig 7. Schematic of nanotriangle fabrication. An oxygen plasma treated polyolefin (PO) film (a) is spun coated with a monolayer of hexagonal closed pack beads (b). The substrate is then coated with a 40 nm layer of gold using chemical vapor deposition, followed by sonication release beads, yielding an array of nanotriangles (c). The substrate is then placed in a convection oven to reduce substrate and size of the nanotriangle array (d).

A modified nanosphere lithography approach was used to fabricate arrays of gold nanotriangles. Polyolefin (PO) films (955-D, Sealed Air Corporation) ,with thickness of approximately 1 millimeter, were laminated onto a 3 millimeter polyester backing, cleaned in isopropyl alcohol, and then dried with pressurized air. The PO film was then oxygen plasma treated for a period of

30 s at a power of 60 W to increase the hydrophilicity of the surface. A 10.1% solid suspension of 500 nm polystyrene (PS) beads in deionized water (Bangs lab) was diluted to a 3:1 ratio with triton X-100 and methanol (1:400 by volume). Approximately 12 µL of this solution was then spin coated onto PO films for 5 minutes at a speed of 1000 RPM. Samples were then allowed to dry for two hours. Afterward, the samples were etched in an Oxygen plasma asher for 15 s at a power of 60 W. First 3 nm Cr adhesion layer and then a 40 nm Au layer were deposited on the samples using electron beam physical vapor deposition, in a Temescale CV-8 ebeam evaporator, to form triangular features in the interstices, as shown in Fig.7. Temperatures did not exceed 115° C during the deposition process to avoid premature shrinking of PO films .The samples were then sonicated in EtoH to release PS beads leaving a metal pattern consisting of triangular features in the regions between the beads. An ice bath was used to avoid deformation of the PO surface during sonication.

Samples were mounted onto glass slides with double sided tape and heated in a convection oven from room temperature to a maximum temperature ranging from 105°C to 135°C. The duration of heating varied at each temperature between 10 and 30 minutes, where the sample was considered to have reduced to its maximum % for that temperature after time periods exceeding 30 minutes. The PO film was kept fastened to a glass slide, with the polyester backing face down, using double side tape during the heating process to ensure uniform heating and to prevent rapid shrinking. Using digital calipers, the size reduction of the length and width of the shrunken PO films were measured for all samples heated to different temperatures. The percentage reduction in size was calculated by taking the ratio of the final length and width of samples relative to the initial dimension for both dimensions, which was measured from the polyester backing, as it does not shrink in heat. Samples were shrunk from 0% up to 77% in

length. In cases where the film shrank asymmetrically, the reduction percentages of both x and y sides were averaged.

Atomic force microscopy (AFM), using an Asylum Research MFP 3D AFM (Santa Barbara, CA) was performed to characterize the resulting topography of samples. 75 kHz resonance frequency probes with diamond-like carbon coating (Budget Sensors-ACST=50) were used for imaging, Scanning electron microscope (SEM) (FEI- Magellan 400 XHR), at ~3 kV, was used to determine the precise change in triangle feature size and periodicity and this measured change in size reduction was compared to the macroscopic size reduction measurements obtained using digital calipers. Reflectance spectra were taken of each sample using a CRAIC micro spectrophotometer 20/20 PV with 100X objective. A background reflectance spectrum was taken using a gold coated PO film.

Surface enhanced Raman scattering (SERS) measurements with a benzenethiol analyte were conducted using a Renishaw Micro Raman system custom built micro-Raman system with laser excitation wavelengths of 532 nm, and 633 nm, respectively. For the 532 nm excitation, integration times were varied from 1 to 10 s, using a laser power of ~2.5 mW. For the 633 nm excitation, integration times from 1s to 30s and power of 600 uW was used. The illumination spot size was 2 μm in diameter, and the objective used for collection was 50X with a 0.75 NA. Samples were immersed in a 10^{-3}M solution of benzenethiol in deionized water for 18 hrs, followed by a methanol rinse to remove excess molecules, leaving a molecular monolayer of benzenethiol on the gold triangles on the surface. A solution of neat benzenethiol was also collected for each laser to provide a standard for enhancement calculations, where

$$EF = (I_{SERS}/N_{SERS})/(I_{neat}/N_{neat})$$

I_{SERS} is the measured intensity of the 998 cm^{-1} benzenethiol peak from the samples with the Au triangles. I_{neat} is the measured Raman signal of a neat benzenethionl solution. The SERS intensity is normalized with laser power, P, and integration time, *t*, such that

$$I_{SERS} = I_{meas}/(P \times t)$$

The neat Raman intensity, I_{neat} is normalized similarly. The number of molecules measured during a Raman measurement, N_{SERS} was found by normalizing the area excited in the laser spot size by the gold coverage of the surface, calculated from SEM images, where

$$N_{SERS} = \rho_{surf} N_A/(f_{Au} A_{spot})$$

The surface coverage of benzenethiol, ρ_{surf} is the molecular packing density on the gold surface, which is reported to be .54 nmol/cm^2, which when multiplied by Avogadro's number, N_A, and divided the spot size, A_{spot} gives the total number of molecules participating in the measurement. This is then normalized by f_{Au}, the gold nanoparticle fractional coverage. To determine the number of molecules measured from the solution,

$$N_{neat} = \rho_{neat} V$$

where ρ_{neat} is the concentration per unit volume of benzenethiol, 9.739 mmol/cm^3 and V is the scattering volume, which can be calculated by multiplying the spot size of the laser by the collection depth, both values measured per instrument.

2.2.2 Results

The nanotriangle arrays, made from nanosphere lithography on a PO film, as described above, were heated at 105°C, 115°C, and 135°C in a convection oven for a period of 10 to 30 minutes. The average macroscopic reduction in x and y dimensions for the films heated at 105°C, 115°C, and 135°C, with respect to the unshrunk samples, were 35%, 52%, and 77%, respectively .

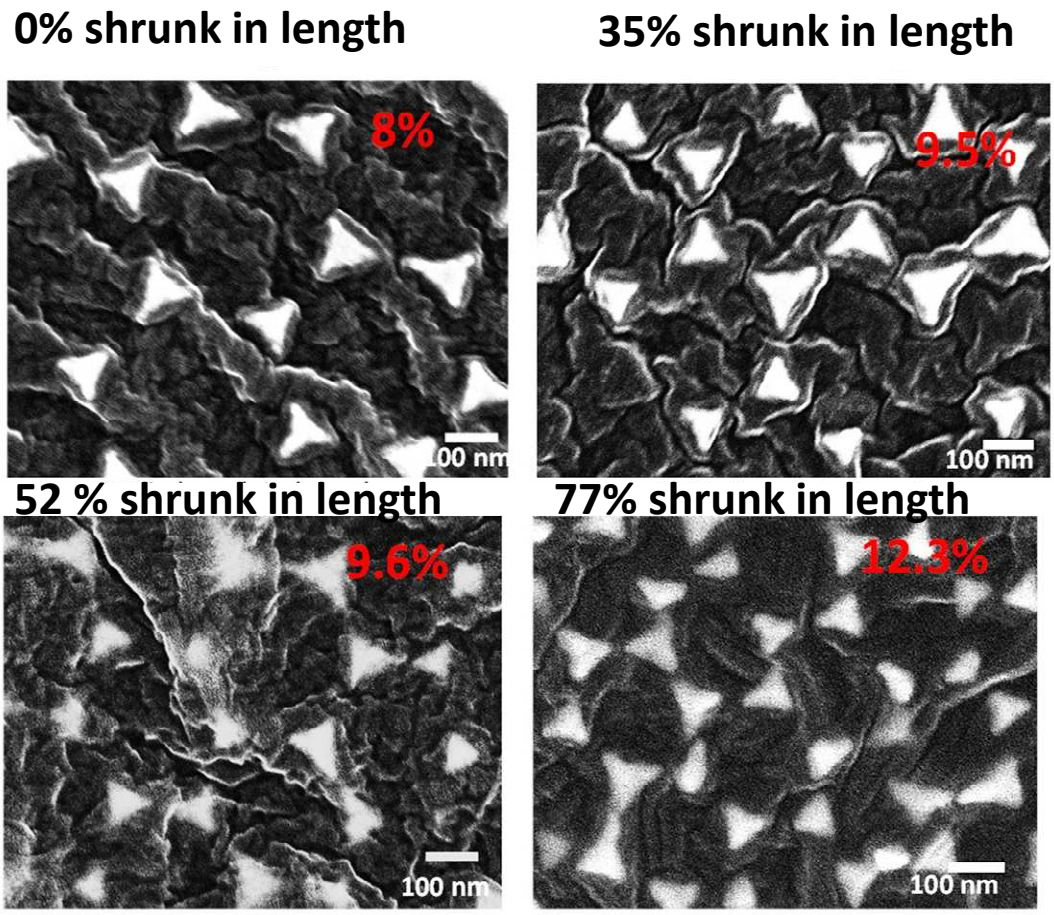

Figure 8. SEM images of nanotriangle arrays on polyolefin film, with average x and y lengths shrunk to 0%, 35%, 52%, and 77% of the original substrate. The percentages shown here are as measured from calipers. In red is the density of gold calculated for each SEM area. The percentages in red show the amount of gold coverage in the area.

Fig. 8 shows scanning electron microscopy (SEM) images of Au nanotriangle arrays on a) PO film that was not annealed, b) annealed at 105°C, c) annealed at 115°C, and d) annealed at 135°C. Etching the microspheres for 15 s is shown to produce triangles with 90 nm base lengths and 95 nm initial tip to tip distances, as shown in Fig 8 a). The initial size and periodicity of the triangles can be varied by changing the etch time of the polystyrene nanosphere mask, where longer etch times result in triangles with smaller base to tip lengths and larger tip to tip distances, as shown in supplemental. The arrays of Fig. 8 exhibit defects in the periodicity of triangular features. Much of the defects arise from the processing conditions that can be optimized to decrease the number of defects. Defects both in HCP sphere arrangement, during spin coating, and metal lift off, during NSL mask removal, are the main sources of imperfections observed in the SEM images of Fig. 8. Due to slight localized variations in the plasma etch rate and metal deposition rate, the unshrunk tip to tip distances and triangle base lengths both vary by ± 14 nm, respectively.

From calculations using the SEM images of Figure 8, the density of Au triangles were found to increase with increased annealing temperature, while the average inter tip distance and triangle base length was found to decrease. When reducing in size from unshrunk to about 35% (Fig. 8 b), the triangles reduce in average base length from 90 nm ± 14 to 85 nm ±14, while the average tip to tip distance reduces from 85 nm ±14to 55 ± 17 nm. From 35% to 52%, the average base length reduces to 77nm ± 16 while the intertip distance reduces to 37 ±16 nm. Finally, from 50% to 77%, the average base length reduces to 60 ±8 nm, while the average tip to tip distance reduces down to 21 nm± 10. Dividing the initial average tip to tip spacing by the final shows a ~75% decrease, which matches closely with the macroscopic 77% measurement. However, the decrease in actual triangle size based on base length, which was not initially

predicted, shows about a 35% reduction after 77% reduction of the macroscopic film, which suggests the shrinking mechanisms of the actual triangles and the periodicity of the triangles are different. It's possible that metal coated PO areas are under tension that leads to differences in size reduction between periodicity and triangle size. It should be noted that the shrinking of the triangular structures does not change the shape of the structure. Once fully reduced, the PO film shows large areas of wrinkling, as shown in Fig. 9, however, nanotriangle areas bigger than 10x10um remain intact for future analysis. This is in contrast to the nanopillars, which were only shrunk up to about 35%, due to excessive wrinkling, when reduced further. This is potentially due to the long oxygen plasma etching used to make the nanopillars, which would result in a larger oxide layer on the film. It also is worth noting that once it reaches a 77% size reduction, the inter tip distances vary from region to region and no longer have the periodicity of the unannealed sample; some tip to tip distances reach about 1 nm. At extreme size reductions the PO film does not shrink uniformly, potentially yielding localized regions where the film shrinks more than the macroscopic measured amount. It is well known that such narrow gap spacings between metallic nanostructures lead to high localized electric fields that are useful for sensing. Thus we examined the optical properties of the samples as a function of annealing temperature.

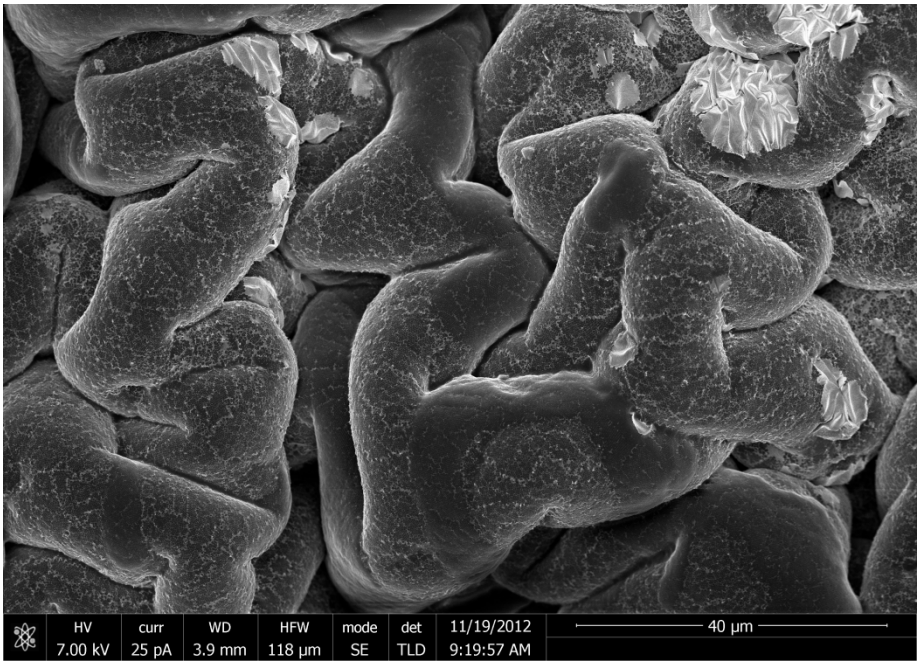

Figure 9. Large view SEM of 77% shrunk nanotriangle arrays.

Fig. 10 shows reflectance spectra for the 0%, 35%, 52%, and 77% reduced arrays, as measured using a CRAIC reflectance spectrometer. Note that the data is normalized with a background subtraction from a spectrum obtained from a gold, non patterned region on the PO substrate to eliminate spectral features resulting from bulk Au. The reflectance spectra shows broad peaks associated with the plasmon resonance of the Au nanostructures for the 52% and 77% reduced structures [39]. Increased variations of the size and periodicity of the Au triangles lead to peak broadening. The peaks shift to lower wavelength with higher percentage of size reduction exhibiting a 100 nm blue shift between the unannealed sample and that annealed at 135° C, which is expected due to decreasing particle size [40].The peak maxima, λ_{max}, shifts from approximately 811 nm, to 777 nm, to 736 nm, to 712 nm, respectively, for the 0%, 35%, 52%,

and 77% reduced arrays.

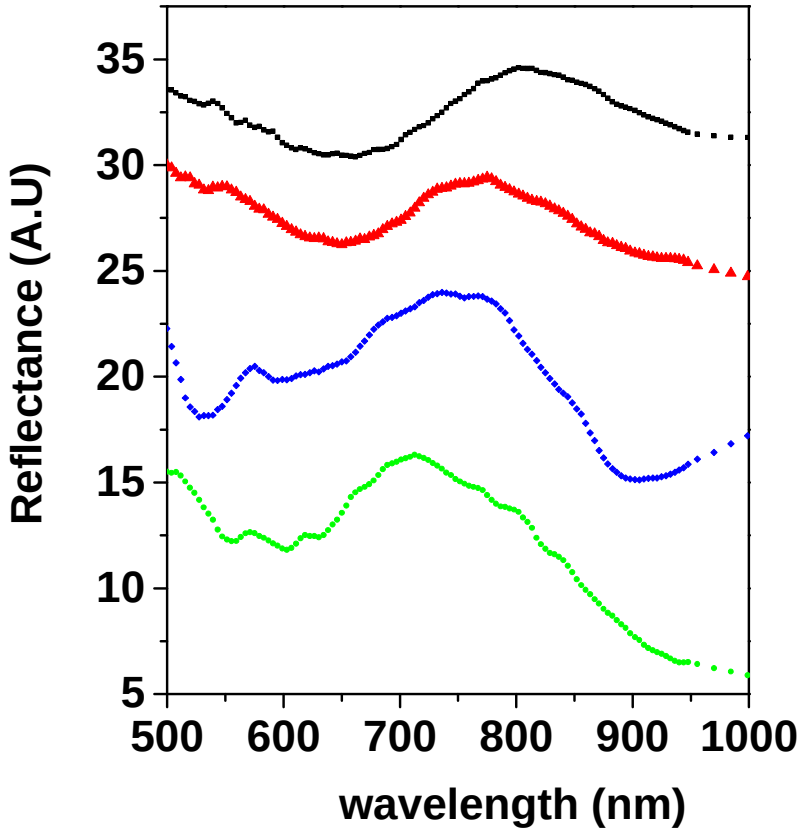

Fig 10. Reflectance spectra for nanotriangle arrays reduced in size by 0%, 35%,52%, and 77%. Spectra are have been overlaid and are shown in arbitrary units.

In order to evaluate how the resulting features and periodicity, due to annealing, affect electric field enhancements, useful for optical detection, the samples were analyzed with surface enhanced Raman scattering (SERS) using a Renishaw Raman microscope with a 785 nm excitation and a custom build Raman microscope with a 633 nm excitation. Fig. 11 shows SERS spectra at 785 nm and 633 nm laser excitation. As shown left in Fig.11, the intensity of the SERS benzenethiol peaks, at 785 nm excitation, first increases with sample size reduction of 35% by about a factor of ten when compared to the unannealed sample. The SERS intensity for

samples with larger size reductions then decreases, with negligible SERS signal observed for the sample reduced by 77%. In the case of 633 nm excitation, negligible SERS signal was observed for the unannealed sample, even when integrating for 30s, while the 35% and 52% shrunk samples both showed measureable signal at 1s and 5s integration times in Fig. 11. The SERS spectra of the 52% reduced array show an approximate tenfold increase in SERS signal when compared to 35 % reduced array. The 77% reduced array has not yet been measured, due to lack of availability of a Raman setup with a 633 nm excitation, but will be measured soon. It is believed that this sample will show highest EF for this excitation, due to spectral positioning of its plasmon resonance, and due to the increased tip to tip distance of the triangles.

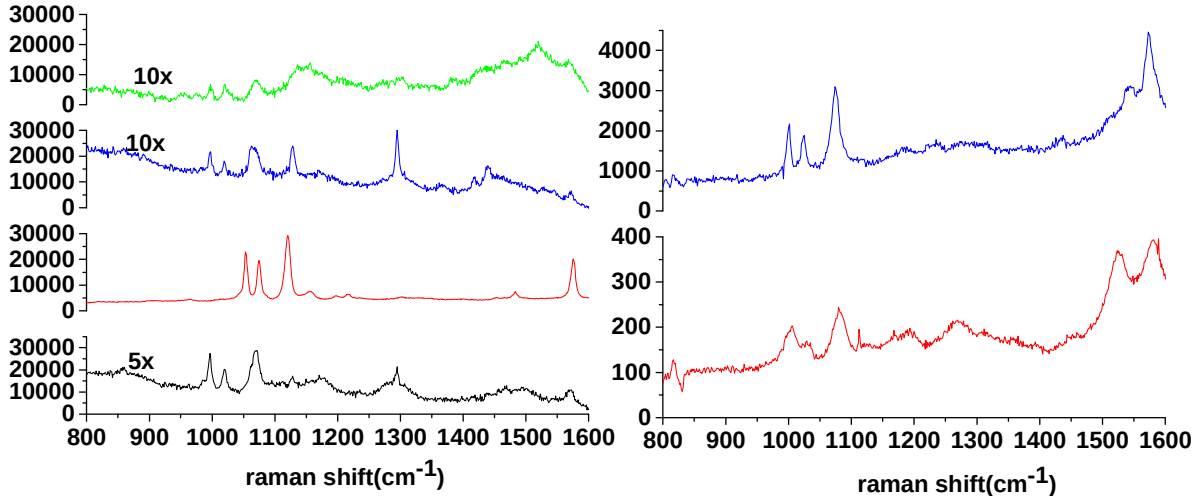

Fig 11. A) SERS spectra of a monolayer of benzenethiol on gold nanotriangle arrays reduced in size by 0%,35%,52%, and 77%, for excitation wavelengths of 785. B) SERS spectra at 633 excitation wavelengths for25% and 50% reduced triangle arrays.

In order to make quantitative comparisons, enhancement factors (EF) were calculated for all the SERS data, using the SERS intensity of the 998 cm^{-1} peak, which represents the C-H out of plane bending vibration mode. Table 2 lists the calculated EFs for the Au triangle arrays as a function

of size reduction and laser excitation. Note that there will be a red shift in the Stokes Raman signal as the molecular vibration absorbs energy during the inelastic scattering event. The scattered wavelength for the 998 cm-1 peak at each laser excitation was calculated from the following equation:

$$\Delta\omega = \frac{1}{\lambda_{excitation}} - \frac{1}{\lambda_{scattering}}$$

For the 785 nm excitation and the 833 nm excitations, the scattered wavelengths were found to be 852 nm and 676 nm, respectively. Table 2 lists the observed, $\lambda_{max,}$ in the reflectance spectra of each sample as this is associated with the plasmon resonance of the Au triangles. As shown in table 2, at the 785 nm excitation, the EF increases as the substrate is reduced by about 35%, reaching a maximum of ~$4x10^7$, but decreases for arrays reduced by further amounts. One would expect the maximum SERS signal when excited/scattered light is near the plasmon resonance. One would also expect higher SERS signals as periodicity of Au triangles decreases. The trend makes sense for the 785 nm excitation, considering that the plasmon resonance blue shifts from about 820 nm to 770 nm as the sample reduces to 30%, and then shifts further away from the excitation wavelength at higher reduction percentages. The only slight discrepancy is the difference in EF between the unshrunk and 30% shrunk samples, where the plasmon resonance of the unshrunk, while slightly red shifted from the excitation wavelength, is slightly closer to the calculated scattering wavelength. This difference can be explained by considering the difference in periodicity between both samples, where the 35% shrunk sample has considerably smaller inter tip distances, resulting in a stronger field. At the 633 nm excitation, no EF was calculated for the 0% reduced sample due to lack of signal, whereas the 35% and 52% samples showed EFs of $7x10^6$ and $3x10^7$, respectively. The increase in EF makes sense, considering the plasmon resonance shifts from 770 nm to 730nm, where the ideal resonance for

the 633 nm excitation would be between 630 nm and 676 nm. Although the plasmon resonance is still outside of this range, the peak is broad enough to still see some enhancements. The EF for the 52% reduced sample at 633 nm excitation, comparable to the EF from the 35% reduced sample when excited on resonance, at 785 nm, which suggests a stronger electric field in the former case, which would be expected, due to smaller feature sizes and higher bowtie density. Most significant, is the ability to tune the spectral location where the nanotriangle array will exhibit the highest SERS EF. This is an unambiguous example of changing the plasmonic properties of an array quickly and at a low cost.

Sample Size Reduction (%)	Λ,PR(nm)	Λ,exc (nm)	EF,998 cm^{-1} (nm)	Λ,exc (nm)	EF,998 cm^{-1} (nm)
0%	810	785	$2.8x10^{6}$	633	-
35%	770	785	$4.0x10^{7}$	633	$7.0x10^{6}$
52%	720	785	$2.3x10^{6}$	633	$3.0x10^{7}$
77%	710	785	$9.0x10^{5}$	633	-

Table 2. Enhancement factors and plasmon resonances are shown for each of the four samples at 785 nm and 633 nm excitations. The calculated scattering wavelengths for the 785nm and 633 nm excitations at the 998 cm^{-1} were found to be 852 nm and 676 nm.

2.2.3 Summary

Nanotriangles have been fabricated using self-assembly onto a polyolefin thermoplastic film. By heating the plastic PO substrate, the average tip to tip spacing of the gold nanotriangle

array has reduced up to 77% and the average base length of the triangles has reduced up to about 33%. The exact extent of this reduction can be controlled by heat temperature. The reduction in geometry and periodicity has shown to blue shift the plasmon resonance, with a tunable window of around 100 nm. SERS spectra for each reduced sample has correlated with the reported plasmon resonances, where the highest calculated EF was $4x10^7$. Perhaps most interesting was that this EF was achievable for both the 785 nm and 633 nm excitations, by simply heating the substrate to the desired % reduction, showing true tunability of the structures. Furthermore, the fully shrunk sample showed localized regions with inter tip distances approaching 1 nm, which may be suitable for hot spots. By incorporating a thermo plastic substrate with self-assembly, structures can be easily modified in terms of structure and optical properties, in addition to potential enhancements in electronic field strength. While studies so far have focused on nanotriangle arrays on PO produced from 500 nm PS microspheres, we have also produced triangles from 250 nm PS microspheres, yielding arrays with much smaller inter tip spacing and triangle feature sizes. In addition to measuring the 633 nm excitation of our current 77% reduced triangle array, the next logical step is to repeat reflectance and SERS experiments for these smaller arrays, which are predicted to have stronger hot spots due to their closer tip to tip distances.

2.4 Summary of nanopillar and nanotriangle structures

By utilizing nanosphere lithography, a tried technique, with the thermal responsive PO film, a new technique, we have achieved the following benefits which are unique to most other bottom up assembly techniques. 1) We have showed independent parameterization of periodicity and structure size, through size reduction of our nanobead-pillar arrays. 2) We have showed size

reduction in both nanopillars and nanotriangles, where the latter structure, requiring minimal plasma etch, can be reduced in interparticle spacing by up to 77%. 3) We have shown the ability to quickly and cheaply tune the plasmon resonance of NSL-based structures, through the exposure of heat using an ordinary convection oven. It is hoped that these benefits, achieved from using a PO substrate, can be used to tailor other plasmonic structures, including those derived from EBL, in order to enhance and optimize optical properties for applications in sensing, and, in the case of EBL, to potentially fabricate new structures at smaller length scales than those currently achievable.

3. Silicon carbide nanostrucctures

Surface phonons are analogous to surface plasmons in their ability to couple with light in the infrared, to create surface phonon polaritons (SPhPs), and also to become localized at the nanostructure [41,42]. Localized optical phonons show some properties similar to localized

plasmons, in that they can be observed as surface vibrations of a lattice at a specific frequency. Optical phonons occur between atoms of different mass and charge, such as silicon and carbon in silicon carbide, and are excited in the mid-infrared to gigahertz spectral region. Like plasmons, these lattice resonances can potentially be tuned to respond at different frequencies in the infrared, based on structure and material. Surface optical phonons have picoscale lifetimes, which are orders of magnitude higher than the scattering times for free carriers supporting plasmon modes in metals and doped semiconductors. Therefore, SPhP materials have a strong potential for low loss nanophotonic devices, in addition to sensing devices that work in the mid to far-IR range. Typical SPhP materials include SiC, III-Ns, III-Vs, and SiO2 [43-46].

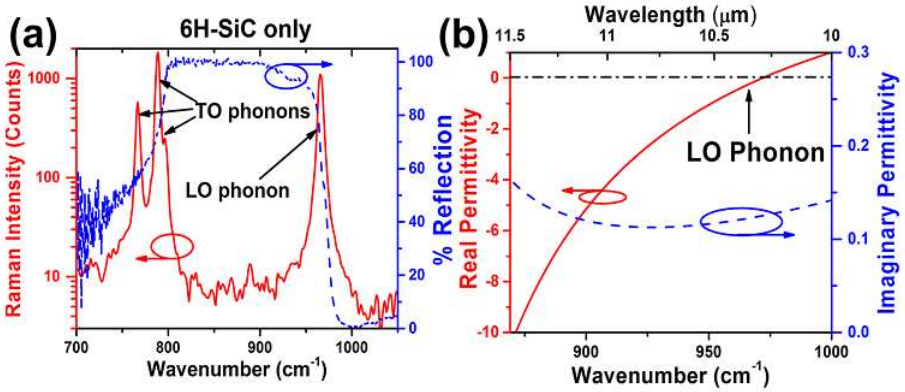

Figure 11 (a) Micro-Raman (red solid line) and FTIR reflection (blue dashed line) spectra of a 300 um 6H−SiC substrate, showing the LO and TO phonon modes within the reflective Restrahlen band. (b) The real and imaginary parts of the permittivity, determined from fitting of the reflection spectra of the 6H−SiC substrate, which was used for nanopillar fabrication. The spectral range provided coincides with that of the position of the LO phonon and the observed localized SPhP modes presented in this work. The horizontal dashed/dotted line shows where the real permittivity is equal to zero [47].

Between the transverse(TO) and longitudinal (LO) optical phonon modes, where the permittivity is negative, the coherent oscillations of the charged lattice can result in screening of

incident light and a spectral region of high reflectance referred to as the Restrahlen band. Shown in Fig. 12 a) are the TO and LO phonon modes revealed by Raman scattering, in red, and the Restrahlen band, in blue, shown from IR reflectance, taken on a 6H-SiC substrate [47]. Fig. 12 b) shows the real and imaginary permittivity of SiC at the same frequencies, taken from fitting of the reflectance spectra of 6H-SiC. The real permittivity becomes negative at the LO phonon mode, and increases in negativity for decreasing energy until reaching a minimum at the TO mode. Within this region, the reflectance of 6H-SiC becomes increasingly close to 100%, demonstrating behavior of a metal. It is in this region that SiC and other dielectric nanostructurs can support tunable, localized SPhP modes. Significantly, the small imaginary part of the permittivity in Fig12 b) shows that losses are small in this region.

Previously, little work has been done to fabricate localized SPhP resonators- in the past, methods such as reactive ion etching (RIE) resulted in damping of the phonon mode response [48]. However in this project, localized SPhP resonators with defined resonate responses were reported. To induce localized SPhP resonant modes, 800 nm tall SiC nanopillar arrays were fabricated with diameters ranging from 150 nm to 260 nm [47]. My specific role in the project was to measure FTIR reflectance of the substrates to determine SPhP modes and SphP mode changes as a function of pillar diameter and pitch, in addition to performing some micro Raman measurements on the substrates. These measurements help show the potential of SiC as a low loss alternative to traditional plasmonic systems.

3.1 Experimental

6H-Silicon carbide substrates about 350 um thick were used. An Al/Cr hard mask, defined by standard electron beam lithography, physical vapor deposition (PVD), and liftoff, was used as an

etch mask. Nanopillars were fabricated using reactive ion etching (RIE) of equal parts pressure ,SF6 and Ar, at 150 W power at room temperature for a duration of 38 minutes. The Al/Cr mask was then removed with wet chemical etchants, followed by a hydrogen atmosphere etch in the growth cell of an Aixtron VP508 growth reactor at 1400° C for 3 minutes, to remove any surface damage induced by the RIE process and to remove any fluorine contaminants. Micro Raman and FTIR spectroscopy were both used to characterize the SPhP resonances of the 6H-SiC nanopillar substrates, of varying diameters and interpillar gaps. Mid-IR reflectance spectra were measured using a Thermo Scientific, Nicolet FTIR continuum Microscope with a 15x, 0.58 NA objective, which illuminates the sample at incident angles between 10-35° off normal, and has a weighted average of 25°, which enabled excitation of both transverse dipolar and monopolar modes of the nanopillars. All spectra were collected at 128 averaged scans and .5 cm^{-1} resolution, with a spatial area of 50x50 um, defined by the internal aperture. An initial background reflection spectrum from a gold film, averaged at 1024 scans, was collected at the same spectral resolution to improve signal to noise. Micro-Raman spectroscopy was performed using a Thermo Scientific DXR Raman Microscope with a 532 nm excitation at 10mW with a 100X .9 NA objective, in confocal mode. The integration time was 5s. 3D Electrodynamic calculations were also performed, using the RF module in the finite-element package of COMSOL. Ellipsometry and reflectance data from the 6H-SiC nanopillar samples were used to determine optical constants, and SEM images were used for geometric dimensions. An incident optical field at 25° was used in the simulations to match that of the FTIR microscope.

3.2 Results

Shown in Fig. 13 [45] is the IR reflection spectrum for 6H-SiC (green), and 6H-SiC (red) periodic arrays of nanopillars with 250 nm diameter, 800 nm height, and 150 nanopillar gaps.

Two SPhP modes are shown at around 910 and 930 cm^{-1}, which are similar to ones observed by Urzomohov et al. [49] from 3C-SiC transmission gratings, with 1-2 um diameter holes. There are an additional two peaks at 882 and 888 cm^{-1}, which are attributed to the splitting of a doubly degenerate bulk phonon. The blue line shows calculated reflectance spectrum using COMSOL Multiphysics software, which is in close agreement to the experimental.

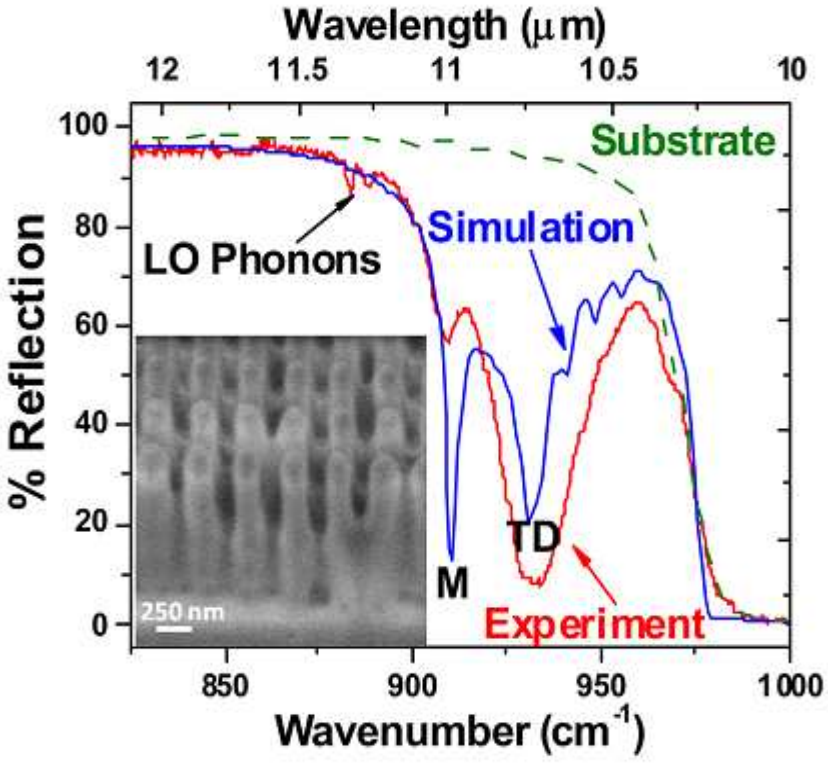

Figure 12 FTIR reflectance spectrum of a periodic array of 800 nm tall, 250 nm diameter, 6H−SiC nanopillars (red solid line) on a 400 nm pitch compared to a simulated (blue solid line) spectrum from COMSOL).“M” and “TD” denote the spectral positions of the monopole and transverse dipole resonances, respectively. The reflection spectrum of the surrounding 6H−SiC substrate (dashed green line) is provided for comparison. An SEM image collected at 45° is shown in the inset [46].

The two modes in the blue line, “M”, and “TD,” are identified as monopolar and transverse dipolar modes, respectively. The IR-reflectance peak at about 930 cm^{-1} was shown to vary with

change in pillar diameter, but was only weakly dependent on angle change and on change in inter pillar gap. The calculated cross sectional and top view electromagnetic field profiles for the 6H-SiC nanopillars coincide with this observation (Fig. 14 a,c), as most of the mode resides in the actual pillar. This mode was shown to be a transverse dipolar mode. This is not the case for the lower energy resonance at around 920 in Fig. 13, depicted as "M," for monopolar, which showed a large dependence on pillar diameter and gap for the IR-reflectance spectra taken. The intensity also increased at larger incident angles. The interpillar gap dependence suggests interpillar coupling. From modeling, it was found that this mode could only be excited from off normal incidence, which suggests it is longitudinal. As shown in Fig. 14 b, the SPhP mode resides within the pillar gaps, around the base of the pillar, which would account for the large pillar gap dependence. In Fig. 14 d, the plan-view electromagnetic profile E_z/E_o calculated for a plane just below the surface suggests that this longitudinal mode is a lower order monopolar resonance. Although the monopolar resonance is not excitable in isolated pillar cases, charge neutrality in this case is achieved by an opposing field near the substrate surface between the nanopillars. Recently, monopolar resonances have been reported in plasmonic nanorods with metal ground planes.

As shown in Fig.14 a,b) the logarithm plots reveal enhancements exceeding well over 5000x, with most of the enhanced field being limited to the surface of the nanostructure, and little of it being inside. The quality factor, Q, defined here as

$$Q = \frac{\omega_{\text{resonant}}}{\omega^{\text{fwhm}}_{\text{resonant}}}$$

or as the resonant frequency divided by the line width of the resonant frequency, was derived experimentally for both monopolar and transverse dipolar resonances, using reflectance spectra

from the 6H-SiC nanopillar substrates of varying diameters, and were found to vary from 40 to 50 for the transverse and from 70 to 135 for the monopolar resonances. These values well exceed those reported for single silver nanoparticles, which showed a theoretical maximum limit of ~40. The high Q factors reported here were expected considering the low losses predicted in Fig. 13 for 6H-SiC nanopillar arrays.

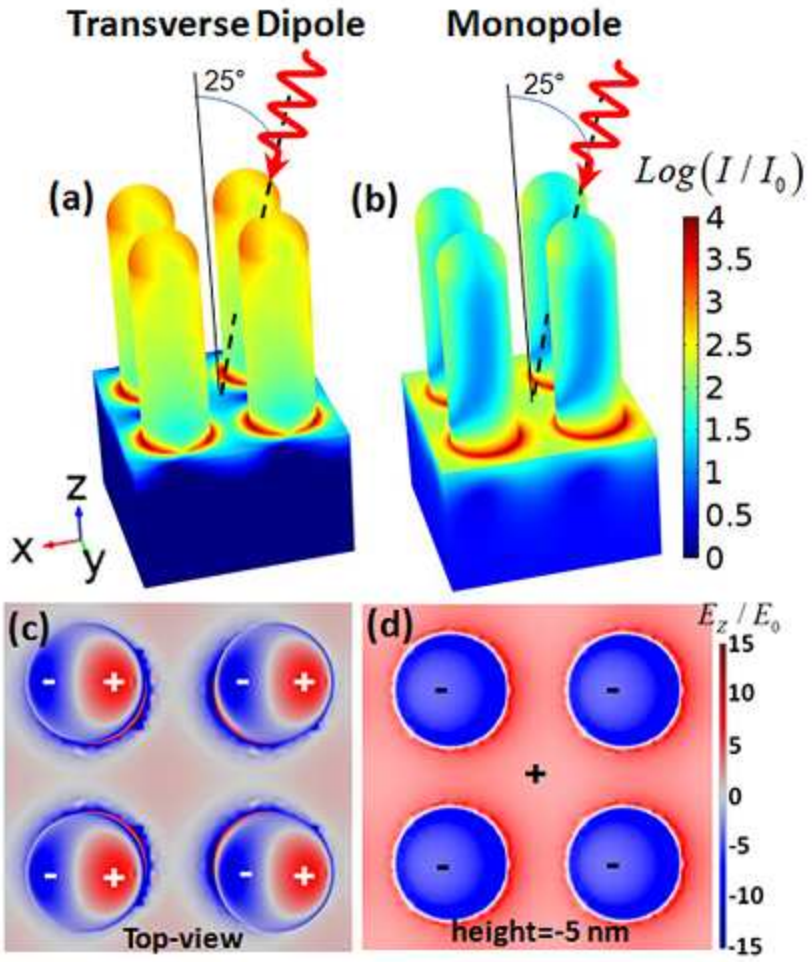

Figure 13 Calculated electromagnetic intensity profiles, log (I/I0), are shown for (a) transverse dipolar and (b) monopolar modes. The angle of incidence of the plane wave used for calculations is at 25°, as depicted. (c) shows the he respective top-view electromagnetic field profile (E_z/E_0), of the transverse dipolar mode and (d) shows the plan-view profile of the monopolar mode, at 5 nm below the substrate surface, which was used to avoid interface effects and to clearly depict the role of the substrate) [46].

Reprinted with permission from J.D. Caldwell, O. J. Glembocki, Y. Francescato, N. Sharac, V. Giannini, F. J. Bezares, J. P. Long, J. C. Owrutsky, I. Vurgaftman, J. G. Tischler, Vi. D. Wheeler, N. D. Bassim, L. M. Shirey, R.

Kasica, and S.A. Maier, "Low-Loss, Extreme Subdiffraction Photon Confinement via Silicon Carbide Localized Surface Phonon Polariton Resonators," *Nano Letters*, vol. 13,no.8,pp. 3690-369, 2013. American Chemical Society.

As with its localized plasmon analogue, modifying the diameter of the 6H-SiC nanopillars was shown to modify the resonance frequency, while keeping a near constant line width. There was about a 4% variation in line width for the TD mode for nanopillar arrays with diameters ranging from 150 nm to 260 nm with a constant nanopillar gap of 150 nm. The lack of variation in line width is most likely from low susceptibility to boundary scattering, due to the short mean free path of the optical phonons, as they have a low group velocity. This is contrary to plasmonic systems which show high susceptibility to boundary scattering losses. Fig. 15 a) shows the experimental FTIR reflectance shifts in localized SPhP resonances, with varying diameter. Fig. 15 b) shows the experimental (closed) and calculated (open) spectral positions of the TD and M modes as a function of diameter. From both the calculational and experimental plots in b), it can be seen that as the nanopillar diameter decreases, the transverse dipolar mode increases in energy, whereas the monopolar mode decreases in energy, where a dramatic shift is seen starting at around a 200 nm diameter. Whereas the TD experimental and calculational curves match to a fairly high degree, there is some discrepancy between the calculational and experimental lines for the monopolar mode, starting at around 878 to 892 cm^{-1}, as shown in the cross hatched region in Fig. 15 b). It is believed that once the monopolar mode is tuned to around this energy, it begins to interfere with the two split LO phonon lines referred to in Fig. 13, resulting in a broadening and asymmetry in the line shape of the monopolar mode, as experimentally observed in the FTIR and demonstrate in 15 a) by the purple arrow. This effect resembles a Fano resonance, where the monopolar mode serves as a broader mode (continuum of states) for the two discrete LO phonon modes.

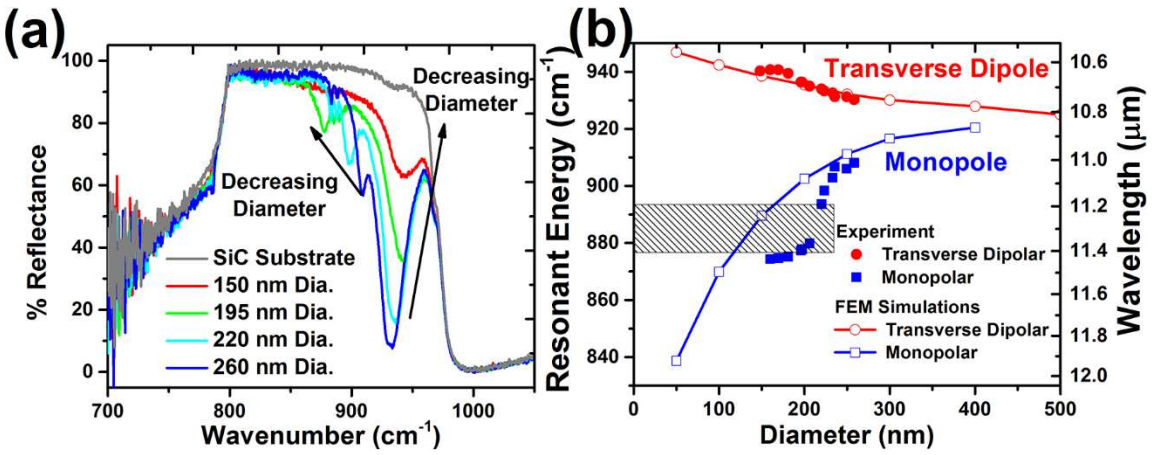

Figure 14(a) FTIR reflection spectra of 800 nm tall, 6H−SiC nanopillars as a function of pillar diameter, in addition to the unpatterned substrate (grey). The arrows show peak shift directions for the two modes with decreasing diameter, in addition to the emerging fano resonance of the downshifting monopolar mode. (b) shows the peak positions for the two modes (red circles and blue squares) as a function of diameter, in addition to calculated values from COMSOL (open symbols, with lines as a guide to the eye). The cross-hatched area marks the spectral region where the monopolar resonance interferes with the LO bulk phonons [46].

Fig. 16 shows Raman spectra from 6H-SiC nanopillar arrays, using a 532 nm excitation (red), in addition to the FTIR reflectance spectra (blue) for a 200 nm diameter nanopillar array with 800 nm height and 350 nm pitch. In many cases, both the monopolar and transverse dipolar modes were found to be Raman active, as the two Raman peaks correlate clearly with the observed FTIR reflectance counterparts. For all arrays measured, the Raman spectra showed a broad surface optical mode centered around 934 cm^{-1}. Both the TD and M localized modes were observed when they resided close to the aforementioned peak, and either decreased in intensity or became unobservable as they shifted away, which suggests that the LSPhP modes are resonantly enhanced by the surface optical mode. Since in most cases the TD mode overlapped with the 934 cm^{-1}mode, it is unclear whether this optical mode is observable in the FTIR,

however, Fig. 15 does show a slight dip in the FTIR reflectance spectrum for a 6H-SiC thin film at 934 cm^{-1}, which may be due to an optical surface mode at the SiC/air interface.

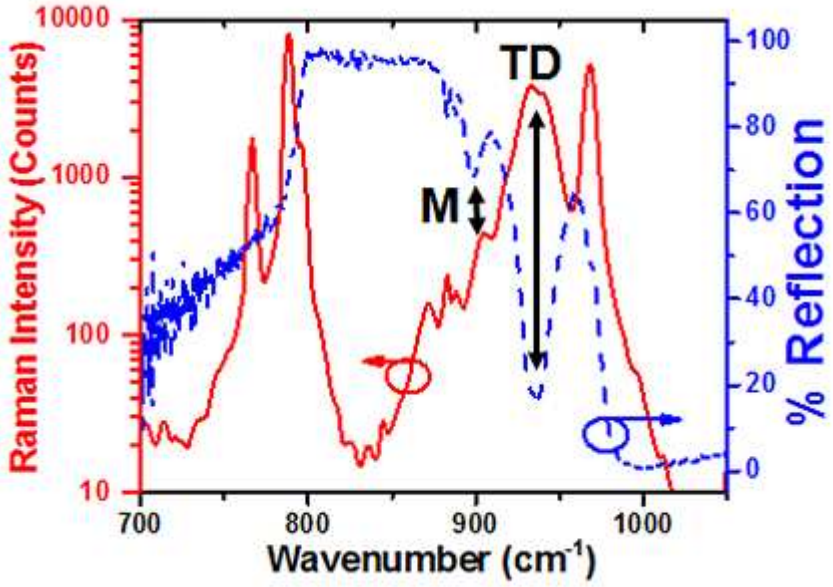

Figure 15. Micro-Raman (red solid line) and FTIR reflection (blue dashed line) spectra from a periodic array of 6H−SiC nanopillars of 200nm diameter, 800 nm height, with a 350 nm pitch. The double-headed arrows correspond to the positions of the two labeled SPhP resonances [46].

Reprinted with permission from J.D. Caldwell, O. J. Glembocki, Y. Francescato, N. Sharac, V. Giannini, F. J. Bezares, J. P. Long, J. C. Owrutsky, I. Vurgaftman, J. G. Tischler, Vi. D. Wheeler, N. D. Bassim, L. M. Shirey, R. Kasica, and S.A. Maier, "Low-Loss, Extreme Subdiffraction Photon Confinement via Silicon Carbide Localized Surface Phonon Polariton Resonators," *Nano Letters*, vol. 13,no.8,pp. 3690-369, 2013. American Chemical Society.

3.3 Summary

Using RIE and a Cr etch mask, 6H-SiC cylindrical nanopillar arrays, with 800 nm pillar height and diameters, ranging from 150 to 260 nm, were successfully fabricated. Despite earlier predicted high signal losses, strong SPhP responses in both FTIR reflectance and Raman spectroscopy were measured. Structuring the SiC surface into nanopillar arrays induced two localized SPhP modes, the transverse dipolar and the monopolar modes, the latter of which is believed to be a modified response of the longitudinal dipolar mode, due to the underlying SiC

substrate. As expected from localized modes, which are analogous to localized surface plasman modes, tuning the pillar diameter, and in some cases interpillar gap of the 6H-SiC nanopillar arrays, shifted the SPhP resonance of the TD and M modes. This shows that, as with plasmonics, SPhP modes can be potentially tuned based on shape, periodicity, and dielectric material of the nanostructures. These SPhP modes are low loss with narrow line widths, with Q factors ranging from 40 to 135. This, combined with localization of these modes, presents nanostructured polar dielectric materials as a potential low loss alternative to plasmonics for nanophotonic and metamaterial devices. The calculated enhancements exceeding 5000x, in addition to the wide spectral position of the Restrahlen band, allow for significant enhancements in molecular sensing in the IR range. Additionally, the interaction of these localized phonon modes with discrete surface SPhP modes can lead to Fano resonances, which have potential use in sensing [50]. The induced monopole and transverse dipolar modes were also found to be Raman active, allowing for complimentary approach to traditional SERS.

References

[1] P. Pattnai, "Surface plasmon resonance," *Applied Biochemistry and Biotechnology*, vol. 126, no. 2, pp 79-92, 2005.
[2]K.A. Willets and R. P. Van Duyne, "Localized Surface Plasmon Resonance Spectroscopy and Sensing," *Annual Review of Physical Chemistry*, vol. 58, pp. 267-297, 2007.
[3] T.R. Jensen,†, M. D. Malinsky, C. L. Haynes, and, and R P. VDuyne* "Nanosphere Lithography: Tunable Localized Surface Plasmon Resonance Spectra of Silver Nanoparticles," *The Journal of Physical Chemistry B*,vol. 104 ,no. 45,pp. 10549-10556, 2000.
[4] J.-Q. Xi, M. F. Schubert, J. K. Kim, E. F. Schubert, M. Chen, S.-Y. Lin, W. Liu, and J. A. Smart, "Optical thin-film materials with low refractive index for broadband elimination of Fresnel reflection," *Nat Photon*, vol. 1, no. 3, pp. 176–179, 2007.
[5] S. A. Maier, "Plasmonics: Metal Nanostructures for Subwavelength Photonic Devices," *IEEE Journal of Selected Topics in Quantum Electronics*, vol. 12, no. 6, pp. 1214–1220, 2006.
[6] E. Ozbay, "Plasmonics: Merging Photonics and Electronics at Nanoscale Dimensions," *Science*, vol. 311, no. 5758, pp. 189–193, 2006.
[7] S. A. Maier, "Plasmonics: The Promise of Highly Integrated Optical Devices," *IEEE Journal of Selected Topics in Quantum Electronics*, vol. 12, no. 6, pp. 1671–1677, 2006.
[8] S. Lal, S. Link, and N. J. Halas, "Nano-optics from sensing to waveguiding," *Nat Photon*, vol. 1, no. 11, pp. 641–648, Nov. 2007.
[9] S. A. Maier, P. E. Barclay, T. J. Johnson, M. D. Friedman, and O. Painter, "Low-loss fiber accessible plasmon waveguide for planar energy guiding and sensing," *Applied Physics Letters*, vol. 84, no. 20, pp. 3990–3992, 2004.
[10] J. N. Anker, W. P. Hall, O. Lyandres, N. C. Shah, J. Zhao, and R. P. Van Duyne, "Biosensing with plasmonic nanosensors," *Nat Mater*, vol. 7, no. 6, pp. 442–453, 2008.
[11] X. Huang, S. Neretina, and M. A. El-Sayed, "Gold Nanorods: From Synthesis and Properties to Biological and Biomedical Applications," *Advanced Materials*, vol. 21, no. 48, pp. 4880–4910, 2009.
[12] H. A. Atwater and A. Polman, "Plasmonics for improved photovoltaic devices," *Nat Mater*, vol. 9, no. 3, pp. 205–213, 2010.
[13] S. J. Lee, Z. Guan, H. Xu, and M. Moskovits, "Surface-Enhanced Raman Spectroscopy and Nanogeometry: The Plasmonic Origin of SERS," *J. Phys. Chem. C*, vol. 111, no. 49, pp. 17985–17988, 2007.
[14] K. Aslan, I. Gryczynski, J. Malicka, E. Matveeva, J. R. Lakowicz, and C. D. Geddes, "Metal-enhanced fluorescence: an emerging tool in biotechnology," *Current Opinion in Biotechnology*, vol. 16, no. 1, pp. 55–62, 2005.
[15] D.-K. Lim, K.-S. Jeon, H. M. Kim, J.-M. Nam, and Y. D. Suh, "Nanogap-engineerable Raman-active nanodumbbells for single-molecule detection," *Nat Mater*, vol. 9, no. 1, pp. 60–67, 2010.
[16] D. Punj, M. Mivelle, S. B. Moparthi, T. S. van Zanten, H. Rigneault, N. F. van Hulst, M. F. García-Parajó, and J. Wenger, "A plasmonic /`antenna-in-box/' platform for enhanced single-molecule analysis at micromolar concentrations," *Nat Nano*, vol. 8, no. 7, pp. 512–516, 2013.
[17] Y. B. Zheng, L. Jensen, W. Yan, T. R. Walker, B. K. Juluri, L. Jensen, and T. J. Huang, "Chemically Tuning the Localized Surface Plasmon Resonances of Gold Nanostructure Arrays," *J. Phys. Chem. C*, vol. 113, no. 17, pp. 7019–7024, 2009.

[18] J. B. Jackson and N. J. Halas, “Surface-enhanced Raman scattering on tunable plasmonic nanoparticle substrates,” *PNAS*, vol. 101, no. 52, pp. 17930–17935, 2004.
[19] E.J Blackie, E. C. Le Ru, M. Meyer, P.G. Etchegoin, "Surface Enhanced Raman Scattering Enhancement Factors: A Comprehensive Study," J. *Phys. Chem. C* ,vol. 111 ,no. 37,pp. 13794–13803, 2007.
[20] J. R. Cole and N. J. Halas, “Optimized plasmonic nanoparticle distributions for solar spectrum harvesting,” *Applied Physics Letters*, vol. 89, no. 15, pp. 153120–153120–3, 2006.
[21] K.-H. Kim and Q-Han Park, “Perfect anti-reflection from first principles,” *Sci Rep*, vol. 3, 2013.
[22] C. Vieu, F. Carcenac, A. Pépin, Y. Chen, M. Mejias, A. Lebib, L. Manin-Ferlazzo, L. Couraud, and H. Launois, “Electron beam lithography: resolution limits and applications,” *Applied Surface Science*, vol. 164, no. 1–4, pp. 111–117, 2000.
[23] V. R. Manfrinato, L.Zhang, D. Su, H. Duan, R.G. Hobbs, E. A. Stach, and K. K. Berggren “Resolution Limits of Electron-Beam Lithography toward the Atomic Scale”
Nano Letters vol. 13, no. 4,pp. 1555-1558, 2013.
[24]H. Lee, J.D Carter, T.H Labean, “Nanofabrication by DNA self assembly,”*Sciencedirect*, vol.12, no.5, pp. 24-32, 2009.
[25] A. Kosiorek ,† W. Kandulski ,† P. Chudzinski ,‡ K. Kempa ,§ and M. Giersig *† “Shadow Nanosphere Lithography,” ,*Nano Lett*. vol. 4, no. 7, pp. 1359-1363,2004.
[26] S. Ji, J. Park, and H. Lim, “Improved antireflection properties of moth eye mimicking nanopillars on transparent glass: flat antireflection and color tuning,” *Nanoscale*, vol. 4, no. 15, pp. 4603–4610, 2012.
[27] J.B Khurgin, G. Sun, “Scaling of losses with size and wavelength in Nanoplasmonics,” *Appl. Phys*. Lett., 99, pp. 211106, 2011.
[28]R. Hillenbrand, T. Taubner, and F. Keilmann. “Phonon enhanced light matter interaction at the nanometer scale,” *Nature. Vol. 418 pp. 159-162, 2002.*
[29] D. Nguyen, D. Taylor, K. Qian, N. Norouzi, J. Rasmussen, S. Botzet, M. Lehmann, K. Halverson, and M. Khine, “Better shrinkage than Shrinky-Dinks,” *Lab Chip*, vol. 10, no. 12, pp. 1623–1626, 2010.
[30] N. Sharac, H. Sharma, M. Khine, R. Ragan. “Tunable nano bead arrays on film for controlling propogation of light,” *SPIE proceedings*, vol. 8809, 2013.
[31] X. Wang, M. Li, L. Meng, K. Lin, J. Feng, T. Huang, Z. Yang, and B. Ren “Probing the Location of Hot Spots by Surface-Enhanced Raman Spectroscopy: Toward Uniform Substrates,”
ACS Nano, vol. 8, no. 1, pp. 528-536, 2014.
[32] H. Sharma, D. Nguyen, A. Chen, V. Lew, and M. Khine, “Unconventional Low-Cost Fabrication and Patterning Techniques for Point of Care Diagnostics,” *Ann. Biomed. Eng.*, vol. 39, no. 4, pp. 1313–1327, 2011.
[33] L. Zhang, X. Lang, A. Hirata, and M. Chen, “Wrinkled Nanoporous Gold Films with Ultrahigh Surface-Enhanced Raman Scattering Enhancement,” *ACS Nano*, vol. 5, no. 6, pp. 4407–4413, 2011.

[34] J. D. Caldwell, O. Glembocki, F. J. Bezares, N. D. Bassim, R. W. Rendell, M. Feygelson, M. Ukaegbu, R. Kasica, L. Shirey, and C. Hosten, “Plasmonic Nanopillar Arrays for Large-Area, High-Enhancement Surface-Enhanced Raman Scattering Sensors,” *ACS Nano*, vol. 5, no. 5, pp. 4046–4055, 2011.

[35] K. Asakawa and T. Hiraoka, “Nanopatterning with Microdomains of Block Copolymers using Reactive-Ion Etching Selectivity,” *Japanese Journal of Applied Physics*, vol. 41, no.10, pp. 6112–6118, 2002.
[36] J. S. Mijovic and J. A. Koutsky, “Etching of Polymeric Surfaces: A Review,” *Polymer-Plastics Technology and Engineering*, vol. 9, no. 2, pp. 139–179, 1977.
[37] B. Päivänranta, H. Merbold, R. Giannini, L. Büchi, S. Gorelick, C. David, J. F. Löffler, T. Feurer, and Y. Ekinci, “High Aspect Ratio Plasmonic Nanostructures for Sensing Applications,” *ACS Nano*, vol. 5, no. 8, pp. 6374–6382, 2011.
[38] Z. Dai, X. Xiao, L. Liao, J. Zheng, F. Mei, W. Wu, J. Ying, F. Ren, and C. Jiang, “Large-area, well-ordered, uniform-sized bowtie nanoantenna arrays for surface enhanced Raman scattering substrate with ultra-sensitive detection,” Appl. Phys. Lett., vol. 103, no. 4, pp. 041903, 2013.
[39] N. Anker, W. P. Hall, O. Lyandres, N. C. Shah, J. Zhao, and R. P. Van Duyne, “Biosensing with plasmonic nanosensors,” Nat. Mater., vol. 7, no. 6, pp. 442–453, 2008.
[40] S. Raza, W. Yan, N. Stenger, M. Wubs, and N. A. Mortensen “Blueshift of the surface plasmon resonance in silver nanoparticles: substrate effects,” *Optics Express*, vol. 21, no. 22, pp. 27344-27355, 2013.
[41] R.H. Ritchie, “Plasma Losses by Fast Electrons,” *Phys. Rev. Lett.*, 106, pp. 874−881,1957.
[42] S. Shen, A. Narayanaswamy, and G. Chen, “Surface Phonon Polaritons Mediated Energy Transfer between Nanoscale Gaps,”*Nano Letters*, vol. 9, no.8, pp. 2909-2913, 2009.
[43]S.S. Ng, Z. Hassan, A. Hassan, “Experimental and theoretical studies of surface phonon polariton of AlN thin film,” *Appl. Phys. Lett*. vol. 90, no.8, 2007.
[44] S.A Holmstrom, T.H Stievater, M. W. Pruessner, D. Park D,
W. S. Rabinovich, J. B. Khurgin, C. J. K. Richardson, S. Kanakaraju, L. C.
Calhoun, R. Ghodssi, “Guided-mode phonon-polaritons in suspended waveguides,” *Phys. Rev*. B, 86, pp. 165120, 2012.
[45] N. Dahan, A. Niv, G. Biener, V. Kleiner, E. Hasman, “Space-variant polarization manipulation of a thermal emission by a SiO2 subwavelength grating supporting surface phonon-polaritons,” *Appl.Phys. Lett*. 86, pp. 191102, 2005.
[46]A. K. Hafeli, E. Rephaeli, S. H. Fan, D. G. Cahill, T. E. J. Tiwald, “Temperature dependence of surface phonon polaritons from a quartz grating,” *Appl. Phys.* , 110, pp. 043517,2011
[47] J.D. Caldwell, O. J. Glembocki, Y. Francescato, N. Sharac, V. Giannini, F. J. Bezares, J. P. Long, J. C. Owrutsky, I. Vurgaftman, J. G. Tischler, Vi. D. Wheeler, N. D. Bassim, L. M. Shirey, R. Kasica, and S.A. Maier, “Low-Loss, Extreme Subdiffraction Photon Confinement via Silicon Carbide Localized Surface Phonon Polariton Resonators,” *Nano Letters*, vol. 13,no.8,pp. 3690-369, 2013.
[48] N. Ocelic, R. Hillenbrand, “Subwavelength-scale tailoring of surface phonon polaritons by focused ion-beam implantation,” *Nat. Mater.*, 3, pp. 606−609,2004.
[49] B. Neuner III, D. Korobkin, C. Fietz, D. Carole, G. Ferro, and G. Shvets, "Critically coupled surface phonon-polariton excitation in silicon carbide," Opt. Lett. 34, pp. 2667-2669, 2009.
[50] S. Zhang, K. Bao, N. J. Halas, H. Xu, and P. Nordlander, “Substrate-Induced Fano Resonances of a Plasmonic Nanocube: A Route to Increased-Sensitivity Localized Surface Plasmon Resonance Sensors Revealed,”
Nano Letters, vol. 11, no. 4, pp. 1657-1663,2011.